Fano-resonant metasurfaces for virus sensing application

Kushagra Shrivastava[1], Chu Hong-Son[2]

[1]H3 Student, National Junior College
[2]Department of applied nanophotonics and plasmonics, Institute of High-Performance Computing

Abstract

The world is plagued by the SARS-CoV-2 pandemic. With more than 5 million deaths to date and new variants rapidly mutating, it has become crucial to be able to quickly detect the virus. RT-PCR is the most commonly used method for virus detection; however, it is prone to false results and is slow. Thus, optical metasurface based sensors are being utilized to detect viruses such as COVID-19 among others. In this report, we investigate a Fano resonance-based periodic structure, etched Si chip metasurface sensor, initially described in Yang et al.'s work which can detect very minute changes in local refractive index. We conducted virtual experiments on the size of the etched square on the Si chip, and the thickness of the Si chip. It was discovered that a side length of 160 nm with a thickness of 120 nm can be used to achieve a very sensitive sensor. This sensor was able to reach the highest sensitivity of 229.46 nm/RIU with FOM of 59.02 at the second resonant mode. In the same environment, we also proposed to explore other designs, such as Si and Au nanohole arrays, for comparison. Si nanohole array was able to achieve resonance, however, the resonant shift was negligible. Au nanohole array achieved weak LSPR resonance, but the resonance was disrupted with the shift in refractive index, showing nanohole arrays are not useful in this configuration. The periodic etched Si chip metasurface sensor has the potential to be further developed for physical manufacturing and usage.

Introduction

The SARS-CoV-2 pandemic, or the COVID-19 pandemic, has affected our world for two years now. After being first recorded in Wuhan, China [1], the virus rapidly spread across the globe and was declared a global pandemic in March 2020 [2]. It has left the global economy in shatters [3], along with more than 5 million deaths [4]. Thus, it has become a necessity for the world to curb its spread in order to heal itself. Due to its contagious nature [5], detection of the virus vector quickly becomes extremely important.

Currently, detection via Reverse Transcription-Polymerase Chain Reaction (RT-PCR) is being majorly used around the world to detect Covid-19 positive patients [6]. However, it is prone to false-positive and false-negative [7] cases during the early stages of infection, with a single kit costing more than 100 USD and 4–6 hour analysis time [7]. Therefore, other methods are necessary to reduce the test cost and decrease the analysis time, not limited to COVID-19.

In recent years, the usage of optical metasurfaces based biosensors has become popular for virus detection [8][9]. Metasurfaces are planar metamaterial structures with subwavelength thickness, operating at wavelengths ranging from microwave to visible. Metamaterials are composed of periodic subwavelength optical structures that resonantly couple to the electric or magnetic or both components of the incident electromagnetic fields, exhibiting response not found in nature. Using metasurfaces, we can change the amplitude, phase and polarization state of an electromagnetic wave through which, we can control the beam propagation direction and shape of the wavefront [10].

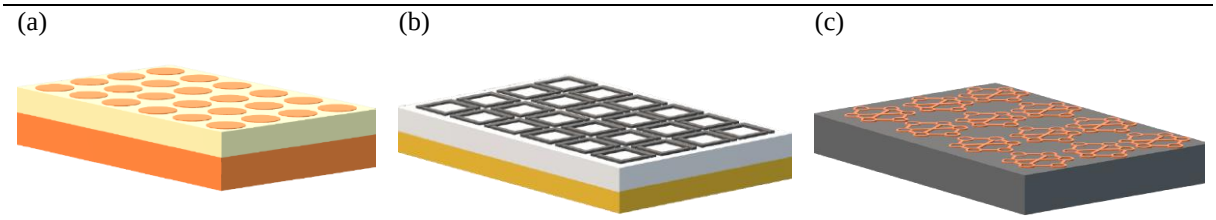

Figure 1: Examples of metasurfaces used for different sensing application. (a) Nanohole array metasurface used for biosensing using microfluids [11]. (b) Polarization based metasurface used for selective virus sensing [12]. (c) Hexagonal structures based metasurface to show anti-proliferation of tumour cells with aspirin [13].

When a target attaches itself to an optical sensor, the effective refractive index of the sensor changes which induces a change of the resonant wavelengths. Metasurface based biosensing is dependent on the shift of these resonant peaks. A sharper and narrower resonant peak is preferred for any sensor as it lets us measure very small peak shifts, giving rise to highly sensitive sensors [14]. Therefore, Fano resonant devices has gained popularity as they can produce multiple resonance responses with very sharp resonance peaks [15].

In general, Fano resonance is a type of resonance that occurs when two oscillators with very different damping rates couple together. One oscillator is almost undamped and changes its phase by π at resonance and the other oscillator is strongly damped which changes its phase slowly. The coupling constant is weaker than the larger damping, which means energy leaks away faster than the transfer of energy between the two oscillators. The interference between the two oscillator modes gives rise to an asymmetrical spectrum with a sharp change between a peak and a dip, as shown in figure 2. The shape of the spectrum is dependent on the phase shift between the two oscillators [15]. For metasurfaces, the two oscillators are called the bright mode, which couples strongly, and the dark modes, which couples weakly, to external radiation such as free space radiation [16].

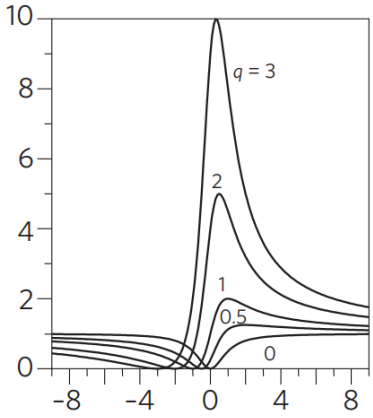

Figure 2: General asymmetrical Fano resonant spectra with different fano factor. The greater the fano factor, the sharper the peak [15].

Fano resonance is being used for various sensing applications. Pathania et al. used it for the detection of antibodies in blood plasma using Plasmonic Nanomatryoshka with sensitivity as high as 244.9 nm/RIU [17]. It has also been employed to build ultrasensitive sensors with sensitivity reaching 926nm/RIU using gold nanoslit arrays [18]. It can even be achieved in other metasurface designs such as nanohole arrays, as shown by Hajebifard et al. in their plasmonic heptamer shaped nanohole arrays, with 400 nm/RIU sensitivity [19]. In some cases, it can even be employed to enhance other kind of resonances, such as Surface Plasmon Resonance (SPR) [20].

Therefore, in this report, we will present Lumerical-FDTD simulations for a fano resonant sensor modified from the design described by Yang et al. [21] and compare its sensitivity to more common designs such as nano-hole arrays. The aim is to create a structure that is highly sensitive to minute changes in refractive index in its local surroundings, so that it is able to quickly detect low concentrations of viruses, including the SARS-CoV-2.

Methodology

All the results presented in this paper are obtained from simulations solved using Finite Difference Time Domain (FDTD) method on Lumerical software. FDTD is a numerical way to solve Maxwell's Equations to find transmittance, reflectance, absorbance, fields, and other results based on a structure. The structures discussed below works on the principle of the resonant peak shifts in the transmission spectrum after a change in the local refraction index.

a. Structure of the periodic etched Si chip on SiO_2 substrate

The structure described below is adopted from the paper by Yang et al. [21], with some modifications in its parameter. The metasurface was an etched Si chip array over a SiO_2 substrate as shown in Figure 3(a). It was modelled as an 800 nm × 800 nm × 800 nm SiO_2 substrate centred at (0, 0, -400) on top of which a 510 nm × 510 nm × 120 nm Si rectangle was placed which was centred at (0, 0, 60). The refractive indices of SiO_2 and Si were extracted from the Handbook of Optical constants for solids [22]. The rectangle was then etched as shown in Figure 3(b) with 4 squares. The side length of square number I and II, d_0, was kept constant at d_0 = 80nm, while side length of square III and IV, d_l, was changed from 20 nm to 170 nm with 10 nm steps. Resonance was not observed outside of this range. The four etchings were centred symmetrically on the silicon chips, with their centres at coordinates (100, 100, 60), (-100, 100, 60), (-100, -100, 60) and (100, -100, 60). The thickness of the etched silicon chip, *h*, was altered from 60 nm to 160 nm with 20 nm step and d_l was kept constant at 160 nm. Outside this range, the resonant peaks were not well-defined.

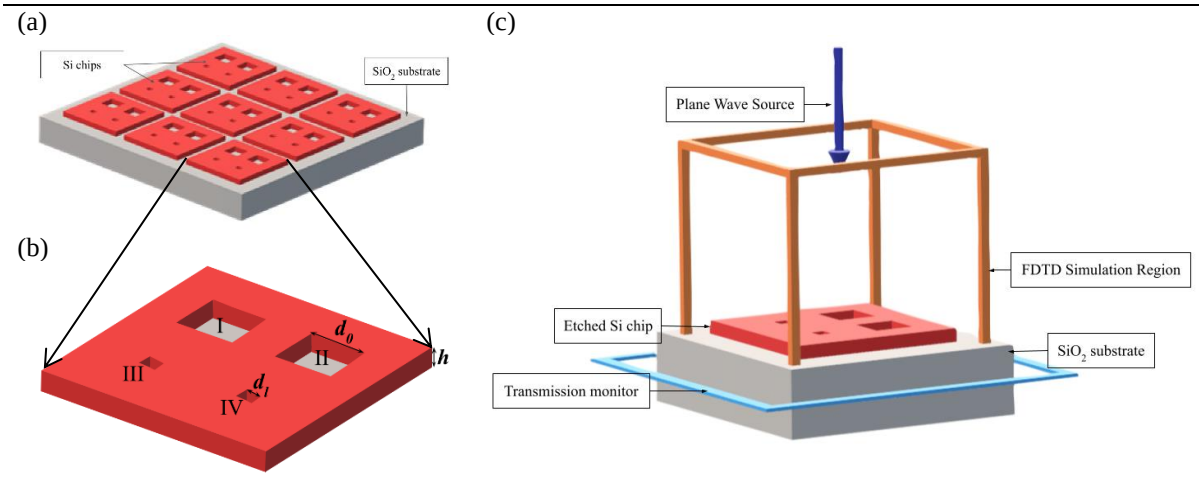

Figure 3: **(a)** Fano resonant metasurface design taken from Yang et al. which is simulated in FDTD. **(b)** Single Si chip from the metasurface. *h* is the height which is changed from 60 nm to 160 nm in steps of 20 nm when $d_o = d_l$ = 80 nm. When *h* and d_0 are kept constant at *h* = 120 nm and d_0 = 80 nm, d_l is changed from 20 nm to 170 nm in steps of 10 nm. **(c)** Labelled FDTD setup which simulates to function as the metasurface in (a).

A 640 nm × 640 nm × 1700 nm FDTD simulation region with its centre at (0, 0, 50) was used. The substrate extends beyond the simulation region in order to prevent divergence error while running the simulations [23]. The simulation time was 2000 fs with 300K and 1.33 background refractive index. Periodic boundary conditions were used along the x-min, x-max, y-min and y-max directions, while Perfectly Matched Layer (PML) boundary conditions were used in the z-min and z-max directions. A finer mesh region of cell size 5 nm × 5 nm × 5 nm was then placed around the etchings with 0 nm buffer. A broadband plane wave source, in the near-infrared wavelengths from 900-1300 nm, was used to inject EM waves along the backward z-axis. It was centred at (0, 0, 775). A frequency domain power monitor was then used to measure the transmission power. Its global monitor was set to record 1000 frequency points and the monitor was centred at (0, 0, -700).

b. Structure of Si nanohole array

In order to compare results, a Si nanohole array, as shown in Figure 4(a), was also created to check whether this structure is more sensitive than the previous one. The parameters of the SiO_2 substrate were the same as described previously. The Si dielectric size was increased in the x and y direction to match that of SiO_2. The thickness was kept constant at 120 nm. A circle was etched in its centre and its radius r was changed from 70 nm to 160 nm, to tune it to achieve Fano resonance. No resonance was observed beyond this range. The dimensions of the FDTD

simulation region were kept the same. Symmetric boundary condition was used in the x-direction and asymmetric boundary condition was used in the y-direction. PML was used in the z-direction. The source and monitor parameters were kept the same.

(a) (b)

Figure 4: **(a)** Silicon nanohole array metasurface design. It was simulated under the same setup as shown in Figure 3(c). **(b)** The design of the single hole used in the simulation. The radius *r* was changed from 70 nm to 160 nm

c. Structure of Gold nanohole array

A gold nanohole array, as shown in Figure 5(a), was also simulated to compare the sensitivity in conditions similar to the previous two structure. All the simulation settings were kept the same as the previous structure except the change of Si substrate to Au substrate, the radius *p* was changed from 90 nm to 180 nm. The refractive indices of Au were extracted from CRC Handbook of Chemistry and Physics [24].

(a) (b)

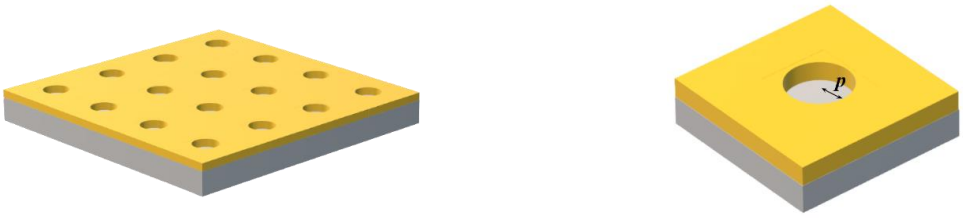

Figure 5: **(a)** Gold Nanohole array metasurface design. Similar simulation setup as shown in Figure 3(c). **(b)** A single cell used in simulation with radius *p* changed from 90 nm to 180 nm.

Beyond the above stated radius, the resonant peaks became too broad.

d. Simulation of the liquid layer on sensors

When virus attaches itself to a sensor, the local refractive index at the surface of the sensor changes. In order to simulate that, a structure group made up of dielectrics with variable refractive index was used. Its dimensions and placement are detailed in Figure 6.

(a) (b)

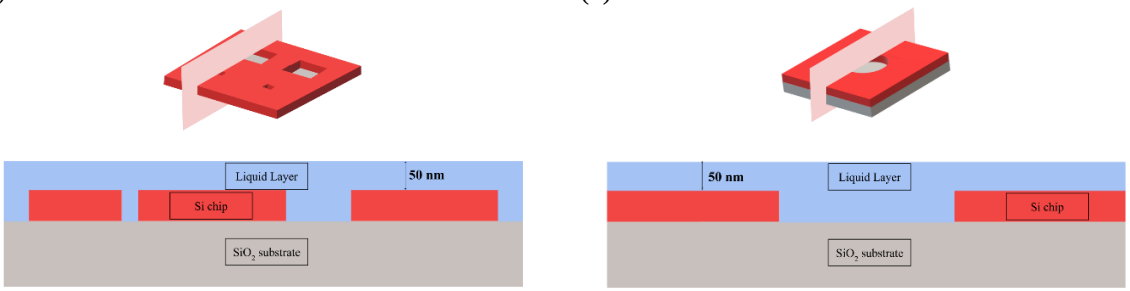

Figure 6: **(a)** Cross section of the Si chip with the liquid. It was simulated as a set of 9 rectangles, with the top rectangle having a constant 50 nm thickness from the sensor surface. Four rectangles were used to cover the sides with water, while the other four rectangles were placed inside the square etchings. The dimensions of the rectangles were altered according to the dimension of the sensor. It was ensured that there was no vacant space between the rectangles and the sensor to simulate fluid filling. **(b)** Cross section of the nano-hole with the liquid. It was simulated as a rectangle, with a constant 50 nm thickness from the sensor surface, and a cylinder which filled in the nano-hole to simulate fluid filling. This was the same for both silicon and gold nano-hole array metasurface.

The refractive index of the liquid layer was first kept constant at 1.34 units, to simulate a change of 0.01 units as the background works at 1.33 units. In order to calculate the sensitivity of the sensor, the refractive index of the liquid layer was increased from 1.34 to 1.40 in 0.01-unit steps. This was used as a proxy for changing concentration of virus on the sensor surface.

Sensitivity, which measures how responsive a sensor is to change in local refractive index changes, was calculated using the formula [25],

$$S = \frac{d\lambda_{resonant}}{dn}$$

A graph of resonant wavelength against the refractive index was plotted, and the gradient of the linear best fit curve was defined as the sensitivity.

The sensitivity was later used to calculate the Figure of Merit (FOM) of the sensor, which is a measure of the resolution of the resonant peaks and its sensing potential [25]. It was calculated by the formula,

$$FOM = \frac{S}{FWHM}$$

Where, S is sensitivity and FWHM is Full width at Half Maximum of the spectrum.

Results and discussion

The results obtained from the simulations as explained in the previous section are detailed in this section. The different resonant peaks will be referred to as numbered modes, which can be seen in Figure 7.

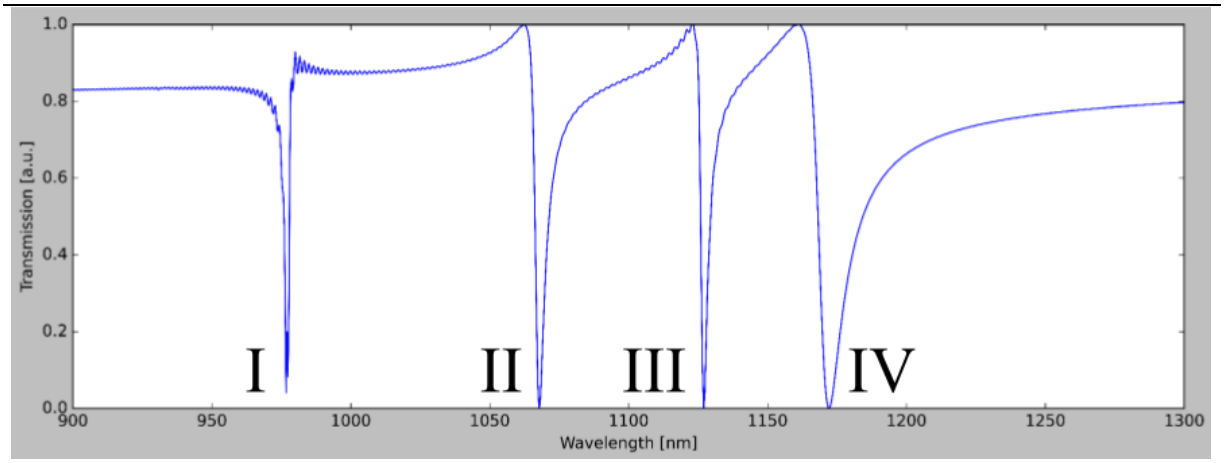

Figure 7: A transmission graph showing different resonant modes. For each experiment, the simulation with the maximum number of modes will be used to number the modes. In this example, the maximum modes were 4, so we will refer to them as I, II, III, and IV mode.

a. Periodic etched Si chip

i. Altering the side length of the square

In this experiment, the size of the side of the square etching is increased from 20 nm to 170 nm. With the increase in length, the transmission profile changes. From 20 nm to 60 nm, the II mode continues to decrease in amplitude. At 70 nm, IV mode appears and II mode vanishes. At 80 mm, only the I and III mode exists. From 90 nm onwards, the IV mode starts increasing in amplitude and from 110 nm, the II mode starts increasing in amplitude. This is because the different modes are based on the symmetry of the metasurface [26]. Mode II and IV are formed when the bright and dark modes leak energy to the free space continuum. As the symmetry of the structure increases, this leakage decreases and thus we only see I and III mode at 80 nm, as $d_0 = d_1 = 80$ nm. As the symmetry further decreases and the size of the two etching continue to increase, interference between the bright and dark mode coupling with the free space radiation causes mode II and IV to reappear as resonant modes but they are broader [26].

However, the focus of this simulation is not to divulge into the shape of the transmission spectra, but rather the resonant shift after the application of the liquid layer which changed the local refractive index with just 0.01 units. As observed figure 8, there was a redshift in the transmission spectra across all the modes and square etching size (Refer to Appendix A for the redshift values). Moreover, as the size of the etching increased, the redshift generally increases until d_l = 160 nm. After that, it decreased across all modes when d_l = 170 nm. Along with that, the modes became wider. As we want the sensor with the greatest resonant redshift possible and narrow resonant peaks for better detection, d_l = 160 nm is the best size to use as the side length of the etched square.

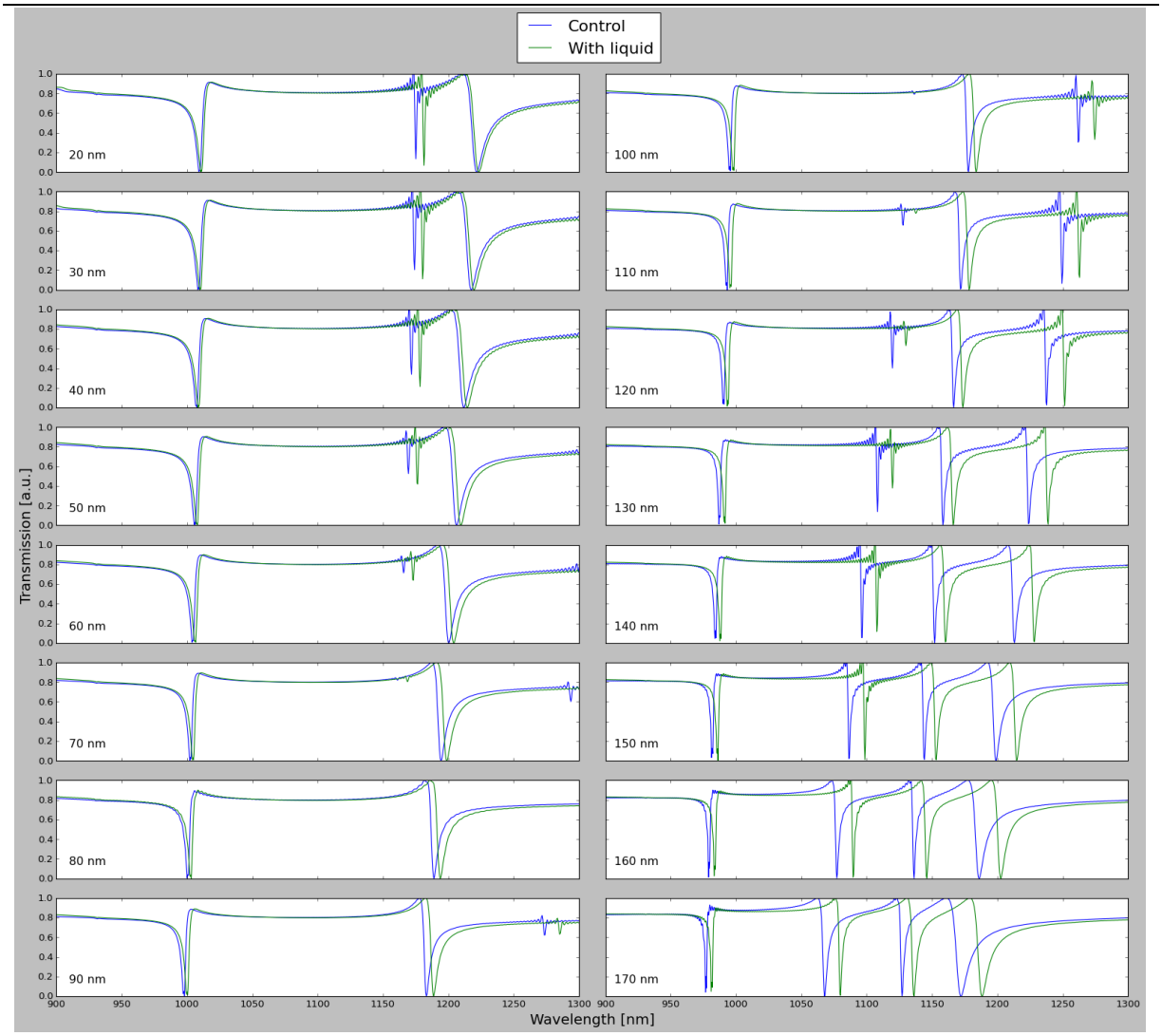

Figure 8: Transmission spectrum as the side of the square etching on the Si chip increases from 20 nm to 170 nm. The change in the structure of the spectrum is clearly visible, as increase in symmetry prevents any leaky channels and only I and III mode remain. Then with the further decrease in symmetry, II and IV modes reappear and continue evolving with wider width. We can also observe the increasing magnitude of the redshift from 20 nm to 170 nm.

ii. *Altering the thickness of the Si chip*

In this experiment, the thickness of the Si chip was altered from 60 nm to 160 nm in 20 nm steps, when d_0 was kept constant at 80 nm and d_l was kept constant at 160 nm. The dimensions were chosen as such because the previous experiment showed them to result in the greatest redshift in transmission spectra. Moreover, this was an unexplored parameter in Yang et al.'s work. It can be observed that with the change in thickness, the transmission spectra undergo heavy redshift. Mode I slowly evolve into a Fano resonant peak after 100 nm thickness and continuously increases in width. The shape of the II, III and IV mode is almost constant throughout the experiment, though it undergoes heavy redshift.

However, after the application of the liquid layer, it is observed that the magnitude of redshift increases with thickness (Refer to Appendix B for the values of redshift). Mode I gain Fano resonant shape after 100 nm only. As the thickness increases, the magnitude of the average redshift also increases at a greater value from 140 nm to 160 nm ($z_{average}$ = 1.61 nm) in comparison to the change from 120 nm to 140 nm ($z_{average}$ = 0.64 nm). However, at 160 nm thickness, the width of the resonant peak has increased. Therefore, it is more feasible to work with either 120 nm or 140 nm thickness as they have similar redshift, but since Yang et al.'s work [21] mentioned that 120 nm is more feasible for manufacturing, it is the preferred thickness. However, 140 nm thickness can be further explored as well in future research.

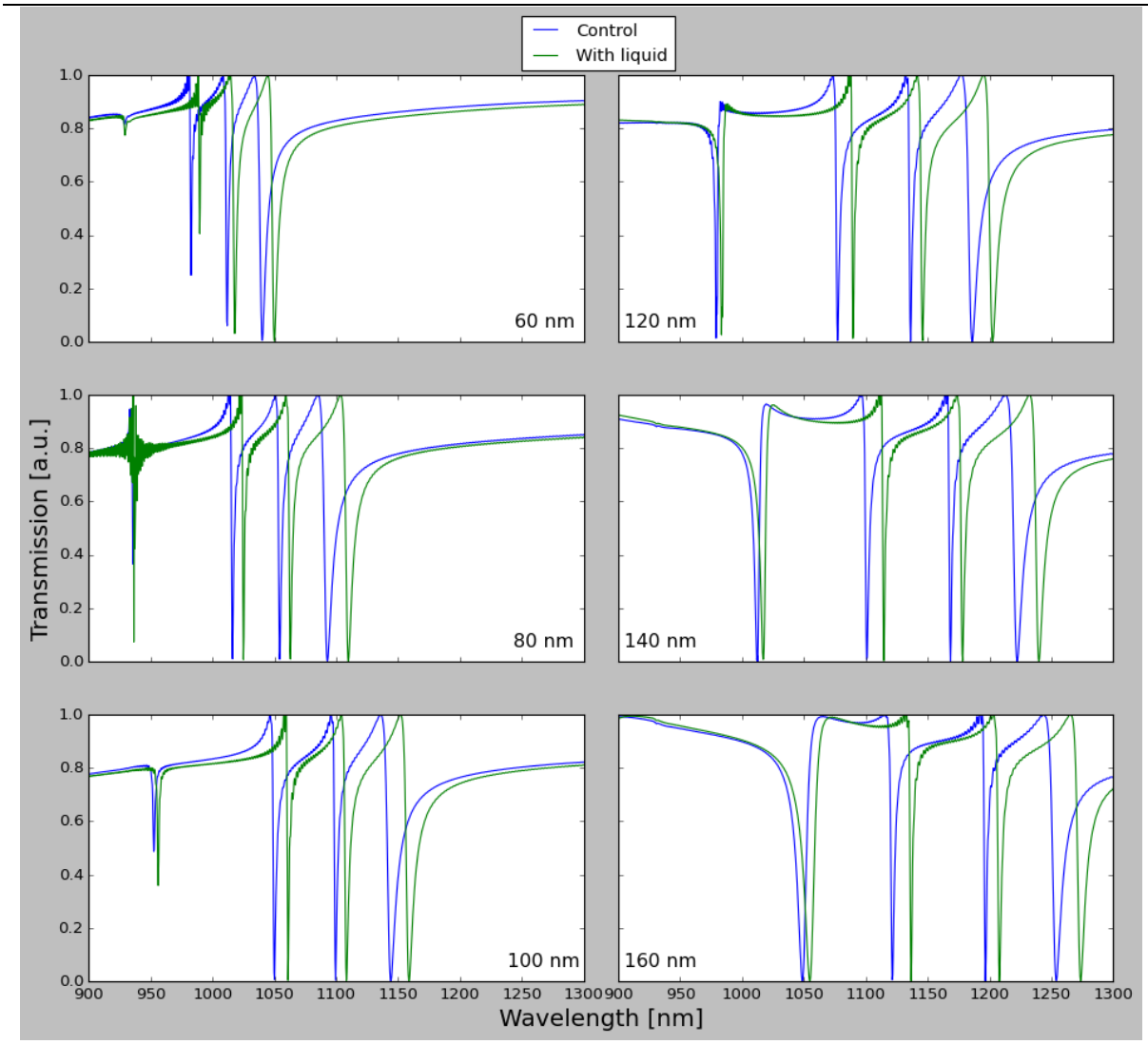

Figure 9: Transmission spectrum of Si chip with varying height (*h*) from 60 nm to 160 nm. The evolution of the I mode is clearly visible along with the redshift of the entire spectrum.

iii. *Altering the refractive index of the liquid layer, sensitivity and Figure of Merit*

From the last two experiments, we were able to observe that a sensor with d_l = 160 nm and h = 120 nm should be the most sensitive. Thus, in order to investigate sensitivity, the refractive index of the liquid layer on top of the sensor was altered from 1.34 to 1.40 in 0.01 unit steps.

Figure 10 shows the redshift bought across by this change for the spectrum, and also for each individual mode. It should be noted that as the mode progresses, the spectrum gets more and more well defined. However, this observation could be due to the computational limitations of Lumerical FDTD. The power monitor records 1000 points between 900 nm and 1300 nm, implying that the data is recorded at approximately 0.4 nm intervals. This brings discontinuity in the spectra. Moreover, the cell size in the mesh region is not set to measure the recording with maximum accuracy. Thus, there are possible inaccuracies in the spectrum.

The resonant wavelength per mode increases as the local refractive index increases from 1.34 to 1.40 (Refer to Appendix C for the values of resonant wavelengths for each mode). This observation is analogous to when a virus sample increases in concentration on the sensor surface, as it also changes the local refractive index on the sensor surface.

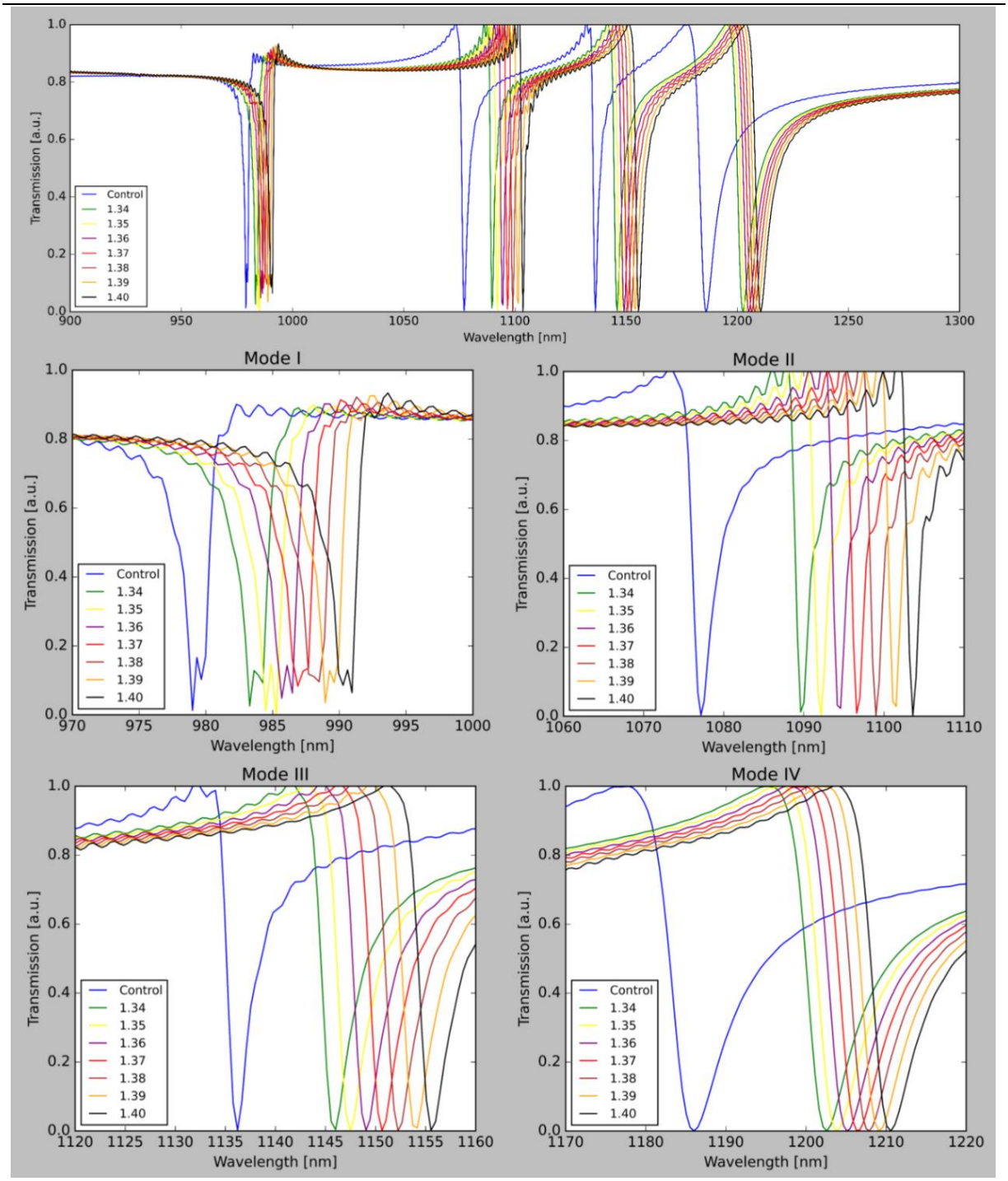

Figure 10: Redshift of the transmission spectrum after changing the refractive index of the liquid layer.

From the redshift of the individual modes, we were able to calculate the sensitivity of each individual mode. The plot of resonant wavelength against refractive index is shown in figure 11. The sensitivity can be calculated as the gradient of the linear best-fit for each individual mode. Sensitivity values of 121.17 nm/RIU, 229.46 nm/RIU, 161.43 nm/RIU and 132.57 nm/RIU were calculated for I, II, III and IV mode, respectively. This implies that mode II, resonating in the range of λ = 1070 nm to λ = 1110 nm, is the most sensitive mode in the near-infrared region for the structure of our sensor.

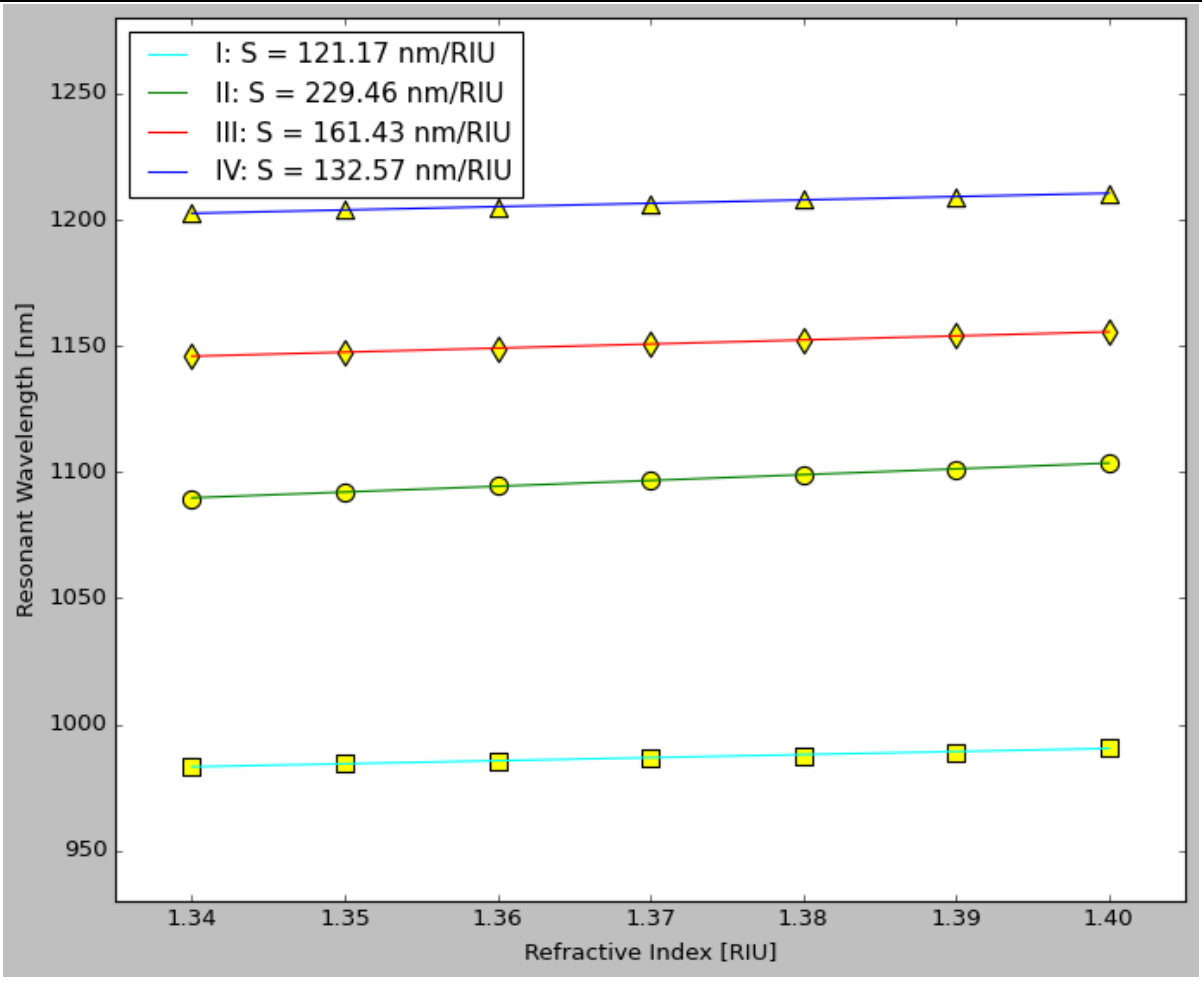

Figure 11: Scatter plot showing the resonant wavelengths across different modes at different local surface refractive index. Squares, circles, diamonds and triangles are datapoints for mode I, II, III and IV respectively. The calculated sensitivity values are mentioned in the legend box. The plot shows green line (Mode II) is the steepest and hence have the greatest gradient and sensitivity.

The corresponding FOM was 57.07, 59.02, 45.78 and 10.72 for I, II, III and IV modes respectively. This shows that Mode II has the highest resolution out of all the four modes, and thus has the best sensing potential.

Even though the structure has a lower performance than the works mentioned before [17][18][19][20], it is easier to manufacture in comparison to the other structures. Fabrication techniques such as Si CMOS is widely used in the industry to manufacture Si wafers and metasurfaces [27] and silicon is a cheaper alternative than other materials such as gold due to its abundance [28]. Given that our structure is aimed to be used at frontlines for virus detection, a cheaper cost and ease of production plays an important role in the selection of the sensor.

b. Nano-hole array metasurfaces

In order to compare and check whether other common designs are more suitable in the simulation environment for periodic etched Si chip metasurface, Si and Au nano-hole arrays were tuned in similar conditions.

As shown in Figure 12, the silicon nanohole array did manage to establish stable Fano-like resonance, however it degraded with the increase in the radius of the nanohole. Moreover, the resonant redshift after the application of the liquid layer is almost negligible. This is because, nanohole arrays use localized surface plasmon resonance (LSPR) instead of fano resonance [29]. Therefore, it is much harder to tune them with these dielectrics and in this wavelength regime.

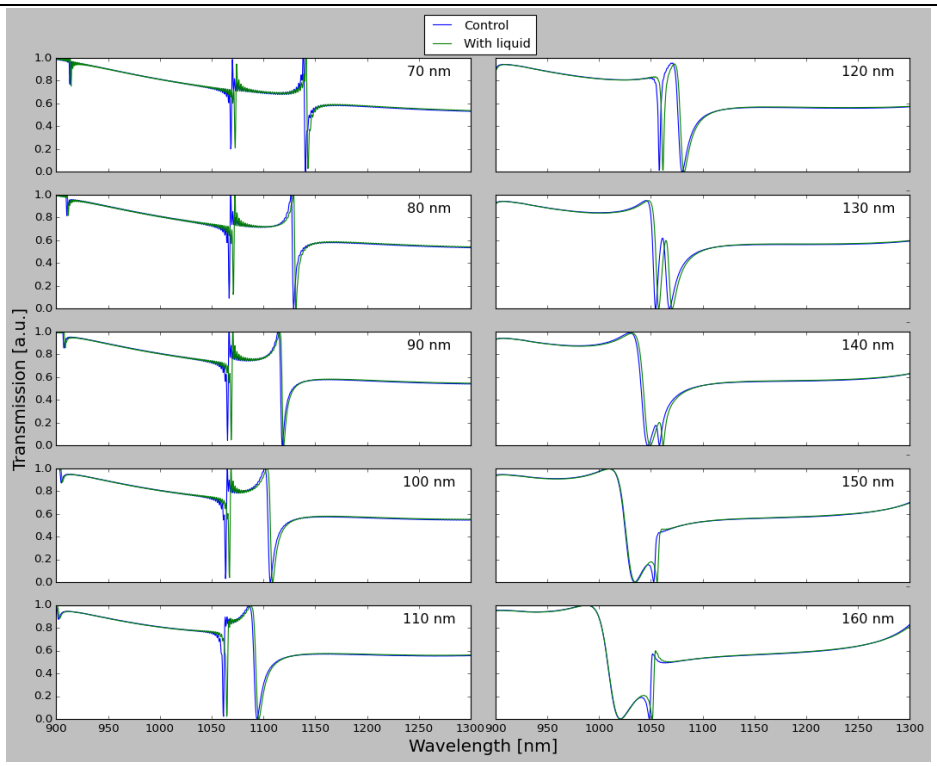

Figure 12: Transmission spectra of the Si nanohole array as the radius was changed from 70 nm to 160 nm

On the other hand, the Au nanohole array managed to achieve LSPR peaks as visible in Figure 13. The amplitude of the peaks increased with the increase in size of the nano-hole, however the peaks became much wider. Thus, the established LSPR was weakly coupled. Moreover, after the application of the liquid layer, the transmission spectrum changes drastically. This clearly displays that nanohole array is not a good design choice here, and we should stick to the originally designed sensor.

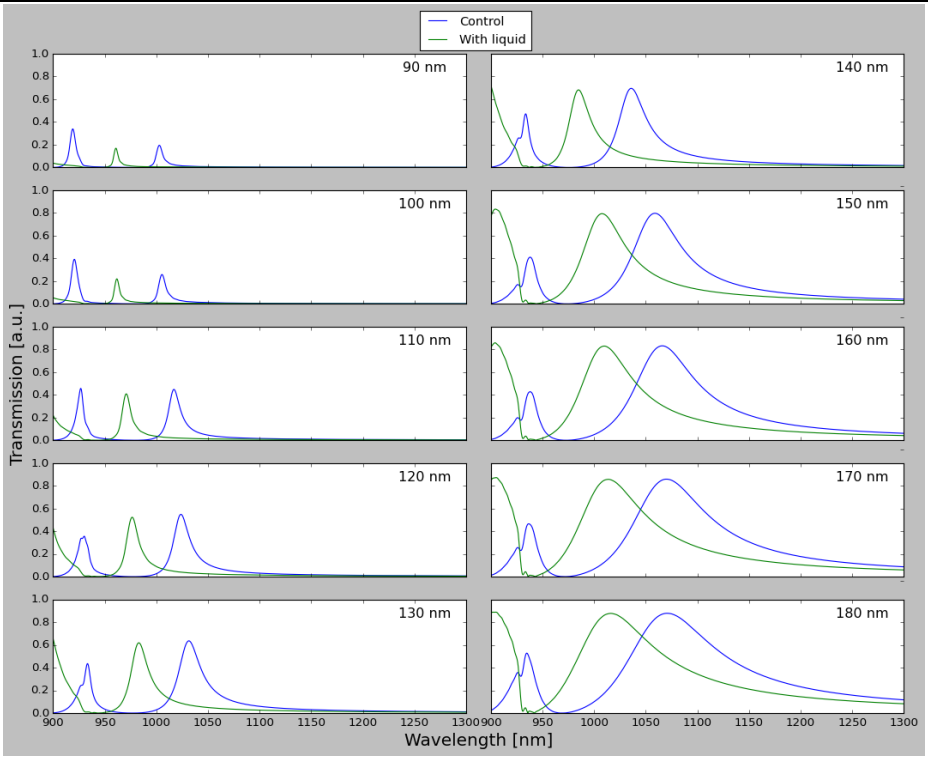

Figure 13: Transmission spectra of Au nanohole array when the radius was changed from 90 nm to 180 nm

Conclusion

From the analysis above, it is clear that a periodic etched Si chip metasurface, with d_l = 160 nm and h = 120 nm is able to achieve the highest sensitivity among all the other parameter permutations. The sensitivity and FOM values are 121.17 nm/RIU, 229.46 nm/RIU, 161.43 nm/RIU and 132.57 nm/RIU, and 57.07, 59.02, 45.78 and 10.72 for I, II, III and IV mode respectively. This shows Mode II is the most sensitive and has the highest sensing potential among all other modes. Therefore, a sensor working in the region of 1070 nm to 1110 nm should give the most accurate results. Moreover, nanohole array designs fail to work in these simulation parameters.

However, there are various available avenues for further research in this area. The actual manufacturing and engineering complications were not explored in this study. The results after manufacturing could differ from the one accounted in this paper due to accuracy limitations with the simulation software. The utilization of this sensor as a mechanical component for medical usage and the ease of usage is also not explored.

Overall, it is possible for a structure as described in this report to function as an actual workable sensor that could help us fight against various viruses, including the COVID-19.

Appendices

Appendix A

The following table shows the resonant redshift for the transmission spectra shown in Figure 8.

d_l / nm	$\Delta\lambda_{resonant}$ per mode / nm			
	I	II	III	IV
20	1.40	6.17	1.54	—
30	1.40	6.17	2.03	—
40	0.69	6.61	3.02	—
50	2.43	7.07	3.49	—
60	2.77	7.02	3.96	—
70	2.07	—	4.41	—
80	3.09	—	4.86	—
90	1.83	—	5.29	11.2
100	2.72	—	5.73	12.7
110	2.03	9.66	6.61	13.5
120	3.37	10.4	7.03	13.8
130	4.69	11.5	7.86	14.5
140	3.66	11.6	8.23	15.3
150	3.31	12.3	9.03	15.9
160	4.28	12.5	9.80	16.6
170	4.26	12.2	9.20	16.2

Appendix B

The following table shows the resonant redshift for the transmission spectra shown in figure 9.

h / nm	$\Delta\lambda_{resonant}$ per mode / nm			
	I	II	III	IV
60	0.296	6.988	5.99	10.09
80	0.8	8.8	8.81	16.82
100	3.542	10.89	8.76	14.43
120	4.28	12.5	9.80	16.6
140	4.33	13.91	9.8	17.7
160	6.39	15.25	11.2	19.33

Appendix C

The following table shows the resonant wavelength for the transmission spectra shown in figure 10 and the FWHM values.

Refractive index / RIU	Resonant wavelength per mode / nm			
	I	II	III	IV
1.34	983.284	1089.61	1146.02	1202.62
1.35	984.484	1092.19	1147.45	1203.90
1.36	985.686	1094.59	1149.05	1205.11
1.37	986.887	1096.60	1150.65	1206.31
1.38	987.688	1099.00	1152.25	1207.91
1.39	988.942	1101.11	1154.17	1209.09
1.40	990.954	1103.61	1155.54	1210.60
FWHM / nm	2.123	3.888	3.526	12.363

References

[1] Page, J. (2021). *In Hunt for Covid-19 Origin, Patient Zero Points to Second Wuhan Market.* Retrieved from https://www.wsj.com/articles/in-hunt-for-covid-19-origin-patient-zero-points-to-second-wuhan-market-11614335404

[2] Adhanom, T. (2020). *WHO Director-General's opening remarks at the media briefing on COVID-19.* Retrieved from https://www.who.int/director-general/speeches/detail/who-director-general-s-opening-remarks-at-the-media-briefing-on-covid-19---11-march-2020

[3] Ozili, P., Arun, T. (2020). *Spillover of COVID-19: Impact on the Global Economy.* Retrieved from https://dx.doi.org/10.2139/ssrn.3562570

[4] Ritchie, H., Mathieu, E., Rodés-Guirao, L., Appel, C., Giattino, C., Ortiz-Ospina, E., Hasell, J., Macdonald, B., Beltekian, D., Roser, M. (2020). *Coronavirus Pandemic (COVID-19)*. Retrieved from https://ourworldindata.org/coronavirus-data

[5] Mohapatra, R., Pintilie, L., Kandi, V., Sarangi, A., Das, D., Sahu, R., Perekhoda, L. *The recent challenges of highly contagious COVID-19, causing respiratory infections: Symptoms, diagnosis, transmission, possible vaccines, animal models, and immunotherapy*. Retrieved from https://dx.doi.org/10.1111%2Fcbdd.13761

[6] Jawerth, N. (2020). *How is the COVID-19 virus detected using real time RT–PCR?* Retrieved from: https://www.iaea.org/bulletin/infectious-diseases/how-is-the-covid-19-virus-detected-using-real-time-rt-pcr#:~:text=This%20technique%20allows%20scientists%20to,detecting%20the%20COVID%2D19%20virus.

[7] Afzal, A. (2020). *Molecular diagnostic technologies for COVID-19: Limitations and challenges*. Retrieved from: https://dx.doi.org/10.1016%2Fj.jare.2020.08.002

[8] GE Healthcare launches next generation Biacore (TM) molecular interaction analysis platform | GE News. (2016). Retrieved from https://www.ge.com/news/press-releases/ge-healthcare-launches-next-generation-biacoretm-molecular-interaction-analysis

[9] Label-Free Silicon Chip based Biosensing – Omega Optics. Retrieved from http://omegaoptics.com/technologies/label-free-silicon-chip-based-biosensing/

[10] Chen, H. T. (2016). *A review of metasurfaces: physics and applications.* Retrieved from: https://doi.org/10.1088/0034-4885/79/7/076401

[11] Escobedo, C. (2013). *On-chip nanohole array based sensing: A review*. Retrieved from: http://dx.doi.org/10.1039/c3lc50107h

[12] Amina, M., Siddiquia, O. Abutarbousha, H. Farhatb, M. Ramzanc, R. (2021). *A THz graphene metasurface for polarization selective virus sensing.* Retrieved from: https://doi.org/10.1016/j.carbon.2021.02.051

[13] Liu, L., Li, T., Liu, Z., Fan, F., Yuan, H., & Zhang, Z. et al. (2020). *Terahertz polarization sensing based on metasurface microsensor display anti-proliferation of tumor cells with aspirin.* Biomedical Optics Express. Retrieved from: https://doi.org/10.1364/boe.392056

[14] Li, Z., Zhu, Y., Hao, Y., Gao, M., Lu, M., Stein, A., Park, A., Hone, J., Lin, Q., Yu, N., (2019) *Hybrid Metasurface-Based Mid-Infrared Biosensor for Simultaneous Quantification and Identification of Monolayer Protein*. Retrieved from: https://doi.org/10.1021/acsphotonics.8b01470

[15] Limonov, M., Rybin, M., Poddubny, A., Kivshar, Y. (2017). *Fano resonances in photonics.* Retrieved from: http://dx.doi.org/10.1038/nphoton.2017.142

[16] Xu, R., Zhang, Z., Wieck, A., Jukam, M. (2020). *Terahertz Fano resonances induced by combining metamaterial modes of the same symmetry*. Retrieved from: https://doi.org/10.1364/OE.383713

[17] Pathania, P., Shishodia, M. (2021). *Fano Resonance-Based Blood Plasma Monitoring and Sensing using Plasmonic Nanomatryoshka.* Retrieved from: https://dx.doi.org/10.1007%2Fs11468-020-01343-z

[18] Lee, K., Huang, J., Chang, J., Wu, S., Weia, P. (2015). *Ultrasensitive Biosensors Using Enhanced Fano Resonances in Capped Gold Nanoslit Arrays*. Retrieved from: https://dx.doi.org/10.1038%2Fsrep08547

[19] Hajebifard, A., Berini, P. (2017). *Fano resonances in plasmonic heptamer nano-hole arrays.* Retrieved from: https://doi.org/10.1364/OE.25.018566

[20] Huang, T., Zeng, S., Zhao, X., Cheng, Z., Shum, P. (2018) *Fano Resonance Enhanced Surface Plasmon Resonance Sensors Operating in Near-Infrared*. Retrieved from: https://doi.org/10.3390/photonics5030023

[21] Yang, L., Yu, S., Li, H., Zhao, T. (2021) *Multiple Fano resonances excitation on all-dielectric nanohole arrays metasurfaces.* Retrieved from: https://doi.org/10.1364/OE.419941

[22] Palik, E. (1985). Handbook of optical constants of solids. Orlando: Academic Press.

[23] Ansys Insight: Diverging Simulations. (2021). Retrieved from https://forum.ansys.com/discussion/25566/ansys-insight-diverging-simulations

[24] Rumble, J. (2021). CRC HANDBOOK OF CHEMISTRY AND PHYSICS (102nd ed.). [S.l.]: CRC PRESS.

[25] Zhang, S., Wong, C., Zeng, S., Bi, R., Tai, K., Dholakia, K., & Olivo, M. (2020). *Metasurfaces for biomedical applications: imaging and sensing from a nanophotonics perspective.* Retrieved from: https://doi.org/10.1515/nanoph-2020-0373

[26] Mi, Q., Sang, T., Pei, Y., Yang, C., Li, S., Wang, Y., Ma, B. (2021). *High-quality-factor dual-band Fano resonances induced by dual bound states in the continuum using a planar nanohole slab.* Retrieved from: https://doi.org/10.1186/s11671-021-03607-x

[27] Li, N., Xu, Z., Dong, Y., Hu, T., Zhong, Q., & Fu, Y. et al. (2020). *Large-area metasurface on CMOS-compatible fabrication platform: driving flat optics from lab to fab*. Retrieved from: https://doi.org/10.1515/nanoph-2020-0063

[28] UCSB Science Line. (2014). Retrieved from http://scienceline.ucsb.edu/getkey.php?key=4527

[29] Barchiesi, D., Kessentini, S., Guillot, N., de la Chapelle, M., & Grosges, T. (2013). *Localized surface plasmon resonance in arrays of nano-gold cylinders: inverse problem and propagation of uncertainties*. Retrieved from: https://doi.org/10.1364/oe.21.002245